Carbon 208 (2023) 148–159

Contents lists available at ScienceDirect

Carbon

journal homepage: www.elsevier.com/locate/carbon

Lithium halide filled carbon nanocapsules: Paving the way towards lithium neutron capture therapy (LiNCT)

Gil Gonçalves [a,b,**], Stefania Sandoval [a], Marina Llenas [a], Belén Ballesteros [c], Tatiana Da Ros [d], Silva Bortolussi [e,f], Laura Cansolino [f,g], Cinzia Ferrari [f,g], Ian Postuma [f], Nicoletta Protti [e,f], Manuel Melle-Franco [h], Saverio Altieri [e,f], Gerard Tobías-Rossell [a,*]

[a] Institut de Ciència de Materials de Barcelona (ICMAB-CSIC) Campus de la UAB, 08193, Bellaterra, Spain
[b] TEMA, Mechanical Engineering Department, University of Aveiro, 3810-193, Aveiro, Portugal
[c] Catalan Institute of Nanoscience and Nanotechnology (ICN2), CSIC and the Barcelona Institute of Science and Technology, Campus UAB, Bellaterra, 08193, Barcelona, Spain
[d] INSTM - Trieste unit - Department of Chemical and Pharmaceutical Sciences, University of Trieste, Via L. Giorgieri 1, 34127, Trieste, Italy
[e] University of Pavia, Department of Physics, Pavia, Italy
[f] Istituto Nazionale di Fisica Nucleare (INFN), The Unit of Pavia, Pavia, Italy
[g] University of Pavia, Department of Clinic-Surgical Sciences, Experimental Surgery Laboratory, Pavia, Italy
[h] CICECO–Aveiro Institute of Materials, Department of Chemistry, University of Aveiro, 3810-193, Aveiro, Portugal

ARTICLE INFO

Keywords:
Lithium-6
Enriched lithium
6Li
Carbon nanohorns
Short multiwall carbon nanotubes
Cancer
Radiotherapy
Nanooncology

ABSTRACT

Neutron capture therapy (NCT) is a form of radiotherapy that exploits the potential of some specific isotopes to capture thermal neutrons and subsequently yield high linear energy transfer (LET) particles, suitable for cancer treatment. Recently, relevant technological improvements have been made in terms of accelerators as suitable neutron sources for NCT at hospitals. However, low selective delivery of current drugs to cancer cells remains as the main challenge for successful clinical application of NCT. This work presents an innovative and previously unexplored approach for the design of nanotherapeutic NCT agents. Herein, a new concept based on carbon nanomaterials that seal ^{6}Li active NCT nuclides is investigated. The ^{6}Li active species are located in the inner cavity of the nanocarrier (carbon nanohorns or carbon nanotubes) and therefore, completely protected from the biological environment, avoiding toxicity and degradation. After encapsulation of the active cargo, the external surface of the nanocarrier is modified for improved biocompatibility. The developed ^{6}Li-filled carbon nanohorns offered the possibility to explore ^{6}Li compounds as active NCT agents by delivering therapeutic doses to cancer cells. We envisage that nanoencapsulation of ^{6}Li can trigger the successful development and implementation of Lithium Neutron Cancer Therapy (LiNCT).

1. Introduction

Cancer is one of the leading diseases worldwide accounting for nearly 10 million deaths in 2020 [1]. Neutron capture therapy (NCT) is a highly effective form of hadron-therapy that exploits the potential of some specific isotopes for cancer treatment, based on the neutron capture and emission of particles. The short range of the particles, comparable to the average cell diameter, produced in NCT can limit the destructive effects to the cells where the isotopes are localized, thus conferring high therapeutic precision to this type of radiotherapy. The recent technological developments that allow the installation of accelerators at medical institutions will bring NCT closer to established clinical applications [2,3].

Since the early days of NCT, many different delivery agents have been developed and studied [4]. However, only two pharmaceuticals have been currently employed in clinical trials, namely sodium mercaptoundecahydro-closo-dodecaborate (BSH; $Na_2^{10}B_{12}H_{11}SH$) and L-BPA ($C_9H_{12}^{10}BNO_4$) derivatives [5,6]. However, over the years the NCT scientific community has focused on the need of new carriers characterized by higher tumour specificity [7–9]. In this respect nanomedicine,

* Corresponding author.
** Corresponding author. Institut de Ciència de Materials de Barcelona (ICMAB-CSIC) Campus de la UAB, 08193, Bellaterra, Spain.
E-mail addresses: ggoncalves@ua.pt (G. Gonçalves), gerard.tobias@icmab.es (G. Tobías-Rossell).

https://doi.org/10.1016/j.carbon.2023.03.034
Received 6 March 2023; Accepted 13 March 2023
Available online 16 March 2023

the application of nanotechnology to medicine, has become one of the most promising routes for the targeted diagnosis and treatment of cancer [10]. Therefore, novel nanocarriers are currently being explored as delivery platforms for NCT, in an effort to overcome the limitations of the classical delivery compounds [11–14].

Despite there is a wide number of nuclides with high affinity for the capture of thermal neutrons, the vast majority of research has been devoted to ^{10}B. Another element that holds great interest for NCT is ^{6}Li. In fact, the nuclear reactions of ^{6}Li resultant from neutron irradiation produce higher energetic particles than the ones resultant from ^{10}B. Therefore the use of ^{6}Li can improve the efficiency of NCT in the eradication of cancer cells.

The particles generated from its capture reaction are high linear energy transfer (LET) particles, following the reaction depicted below. Because of their size and energy, they are confined to a radius of approximately 9–10 μm, comparable to the dimensions of a single cell [15].

$$n + {}^{6}_{3}Li \rightarrow {}^{4}_{2}He(2.05MeV) + {}^{3}_{1}H(2.73MeV)$$

Interestingly, in the early days of NCT, eighty years ago, both ^{6}Li and ^{10}B were considered as potential candidates for NCT [16–18], but shortly after, boron took the leading role and research with lithium was discontinued. The reason most likely resides in the different chemistry of both elements [15]. Boron can form stable bonds with other elements such as carbon, oxygen or nitrogen, thus allowing the synthesis of many different compounds, including boron clusters [19,20]. In contrast, lithium is an alkali metal typically encountered as a cation in inorganic salts and intercalation compounds. Therefore, under biological conditions it would be present as lithium cations. Research with ^{6}Li has thus been very limited. Rudimentary experiments involving crude neutron sources were performed back in the 40s [21]. Despite the scientific limitations on those early studies, a significant increase in tumour regression was observed upon neutron irradiation of a mixture of lithium and boron (using lithium meta-borate) [16]. In a posterior work, Cooper et Zahl investigated the energy absorbed by tissue containing either lithium salts or boron. Even though enriched elements were not available at that time, by extrapolation, they could provide evidence of the potential that ^{6}Li held for NCT [17,18]. Note that naturally occurring lithium is composed by only 4.85% of ^{6}Li.

More recently, in 2010 Louis Rendina addressed the following challenge to the scientific community "can lithium salts herald a new era for neutron capture therapy?" [21]. For the past 70 years, lithium has mostly been utilized to treat bipolar disorder in the clinical setting [22] and it is on the World Health Organization's list of essential medicines [23]. Herein, we intent to expand the use of lithium and provide evidence that lithium (^{6}Li) can indeed herald a new era for NCT. To overcome the limitation that the intrinsic properties of lithium presents to control its biodistribution, lithium salts are sealed in the interior of nanocapsules. The use of nanocapsules offers versatility in terms of biodistribution, because it will be insensitive to the innate affinity of the lithium cation, and it will be merely determined by the physico-chemical properties of the nanocapsules (size, morphology, functional-groups, etc.). Our approach also compensates for the lower cross-section of ^{6}Li *vs.* ^{10}B because a large amount of ^{6}Li is confined in each nanocapsule. This is a paradigm shift in the strategic development of NCT agents, since it will prevent the release of lithium cations in biological media. The possibility of encapsulating a high density of ^{6}Li in the form of inorganic crystals, plus the fact that the nuclear reaction of ^{6}Li with neutrons produces more energetic particles than the ones resulting from ^{10}B, can improve the efficiency of NCT in the eradication of cancer cells.

We will focus on the use of carbon nanomaterials as ^{6}Li nanocarriers, because they are an emerging platform for disease treatment and tissue repair [24–28]. Carbon nanocapsules (CNCs) based on closed-ended filled carbon nanotubes (CNTs), can provide the perfect shelter for the biological stability of high doses of payload [29]. Indeed, filled CNTs have been already successfully explored for high resolution bioimaging [30–32] and more recently for radioisotope therapy [33–35]. In NCT, the employed isotopes are non-radioactive and only become therapeutically active once they are irradiated with neutrons, reducing in this way the risk of secondary effects. In this study, we investigate the nanoencapsulation of enriched ^{6}Li halides into various types of nanocapsules to provide experimental evidence of the potential that the encapsulation of ^{6}Li holds for Lithium Neutron Capture Therapy (LiNCT). Moreover, to the best of our knowledge, this study provides for the first time biological data using isotopically enriched ^{6}Li for NCT.

2. Experimental section

2.1. Material synthesis

2.1.1. Preparation of CNCs from MWCNTs and CNHs

2.1.1.1. Purification, shortening and tip-opening of MWCNTs. The raw multi-walled carbon nanotubes (MWCNTs) used in this work were acquired from NanoAmor. The oxidative cutting of the MWCNTs was performed using a combination of acid treatment and ultrasonication, as previously reported [36]. Briefly, 150 mg of MWCNTs were dispersed in 150 mL of a mixture of H_2SO_4/HNO_3 (3/1) and sonicated during 24 h at a temperature of *ca.* 40 °C. The resulting suspension was washed with distilled water and filtered under vacuum using a 0.2 μm PTFE membrane (Omnipore), until the filtrate reached neutral pH. After that, the MWCNTs were dispersed again in ultrapure water (200 mL) by ultrasonication, and then centrifuged at either 4000 or 20000 rpm (1503 and 37569 rcf respectively) during 30 min. Two different centrifugation speeds were initially employed to assess the degree of removal of large bundles and long carbon nanotubes. The precipitate was discarded (bundles or long nanotubes), and the process was repeated twice. The MWCNTs suspension was collected by vacuum filtration and dried in the oven overnight at 100 °C. Finally, the prepared short MWCNTs were reduced by thermal treatment in order to remove oxygen functional groups introduced during the shortening step. For this purpose, short-MWCNTs (50 mg) were inserted in a silica tube and the sample was left under vacuum for 2 h. The tube was then placed inside a furnace and annealed at 800 °C under vacuum during 2 h (heating rate 3.3 °C·min^{-1}).

2.1.1.2. Oxidizing thermal treatment of CNHs for opening the tips. Carbon nanohorns (CNHs) were acquired from Carbonium. The CNHs were thermally treated at two different temperatures (in order to open the tips and improve the access to the inner cavity) following the protocol described by Utsumi et al. [37]. Briefly, 50 mg of CNHs were placed in a silica boat and then placed in a tubular furnace. The thermal treatment was carried out under dry synthetic air, reaching a maximum temperature of 400 or 500 °C (heating rate of 1 °C·min^{-1}). The samples were immediately cooled down after reaching the maximum temperature.

2.1.2. Synthesis of ^{6}LiI@CNCs

The filling of MWCNTs was attempted with different lithium compounds via molten capillarity wetting, following a modified protocol from the one reported by Sloan et al. for the encapsulation of LiI into single-walled CNTs [38]. Briefly, 10 mg of shortened MWCNTs were mixed with 100 mg of the selected lithium compound inside an Ar filled glovebox (using an agate mortar and pestle), until the sample presented homogenous colour. Subsequently, the powder was sealed under vacuum in a silica tube of *ca.* 10 cm in length. The silica ampoule was placed into a furnace and the mixture was annealed at 5 °C·min^{-1} until reaching the first dwell step (50 °C above the melting point of the corresponding salt: LiI, LiCl and LiF acquired from Sigma-Aldrich with purity >99%). After 4 h, the temperature was increased (5 °C·min^{-1}) up to 1100 °C, where the system was dwelled for 10 min. Finally, the

sample was cooled down (1 °C·min^{-1}) until a temperature 50 °C below the melting point of the inorganic salt and subsequently the cooling rate was increased to 5 °C·min^{-1} until room temperature. This thermal treatment was designed to allow the formation of filled closed-ended carbon nanotubes in a single step [39]. For the filling of CNHs with lithium salts, slight variations to the annealing procedure were applied. The silica ampoule (sealed under vacuum), containing the corresponding mixture (lithium salt/CNHs) was placed inside the tubular furnace and then annealed at 950 °C for 12 h. The system was subsequently cooled down to 600 °C at 1 °C·min^{-1} and finally to room temperature at 5 °C·min^{-1}. Once the best filling rate of CNCs was obtained for LiI, the enriched form of this compound (^{6}LiI) was explored during the NCT studies.

After the filling step, CNCs were purified by washing the excess of inorganic material that remained external to the CNCs. The mixture was first dispersed in water (sonication for 15 min) and then refluxed at 110 °C during 4 h. This cycle was repeated three times, in order to guaranty the complete removal of the excess of non-encapsulated lithium compounds. The purified CNCs were collected by vacuum filtration using a 0.2 μm PTFE Membrane (Omnipore). Afterwards, the sample was dried overnight at 100 °C.

2.1.3. Synthesis of $EuCl_3$@CNCs

The sample of $EuCl_3$@CNHs was prepared following a similar protocol to that described for the encapsulation of lithium halides into CNHs. For that purpose, 15 mg of oxidized CNHs were mixed with 200 mg of $EuCl_3$ and then sealed in a silica tube under an inert atmosphere. The silica ampoule was then placed into a furnace, and the mixture was annealed at 5 °C·min^{-1} until reaching 950 °C. After 12 h, the temperature was lowered to room temperature at a rate of 10 °C·min^{-1}. After the filling step, CNCs were purified by washing the excess of inorganic material that remained external to the CNCs, as previously described.

2.1.4. External surface functionalization of ^{6}LiI@CNCs

The external surface functionalization of the CNCs with free amine groups was performed using diazonium-based arylation reaction [40]. First, the CNCs (20 mg) were dispersed in DMF (20 mL) by ultrasonication during 30 min. After that, 200 mg of 4-[(N-Boc)aminomethyl]aniline were added to the dispersion and dissolved by mechanical stirring. The mixture was cooled down to 0 °C and then 200 μL of isopentyl nitrite were added. The reaction temperature was raised to 80 °C and kept stirring during 4 h. The sample purification was performed by cycles of washing and filtering under vacuum using the following sequence of solvents: DMF/water/methanol/diethyl ether. Finally, the sample was dried under vacuum overnight.

The deprotection of Boc group at the surface of the CNCs was performed by treatment with a 4 M HCl solution in dioxane. The resulting CNCs were initially well dispersed in 20 mL of dioxane solution by ultrasonication during 15 min and then, the dispersion was kept stirring overnight at room temperature. The sample purification was performed by vacuum filtration using the following sequence of solvents: water/methanol/diethyl ether. Finally, the samples were dried under vacuum overnight.

2.2. Characterization

Samples for microscopic characterization were prepared by sonicating a small amount of CNCs in absolute ethanol. The sample was then placed dropwise onto a holey carbon grid. Transmission electron microscopy (TEM) images were obtained using a JEOL 1210 microscope, operating at 120 kV. High resolution TEM (HRTEM), high angle annular dark field scanning transmission electron microscopy (HAADF STEM) and energy dispersive X-ray spectroscopy were carried out in a FEI Tecnai G2 F20 microscope operated at 200 kV coupled to an EDAX super ultra-thin window (SUTW) X-ray detector. Scanning electron microscopy (SEM) images were acquired using a Quanta FEI 200 ESEM FEG microscope operating at 5 kV.

Brunauer-Emmett-Teller (BET) analysis was performed on 15–30 mg of raw CNHs after being annealed at 400 °C or 500 °C dry air. The samples underwent a treatment of adsorbed gas removal at 150 °C for 2 h. This was followed by nitrogen adsorption/desorption.

Thermogravimetric analyses were performed on a Netzsch instrument, model STA 449 F1 Jupiter®, under flowing air at a heating rate of 10 °C·min^{-1}.

Samples for X-ray photoelectron spectroscopy (XPS) were prepared by placing dropwise a dispersion prepared by sonicating the sample in dry ethanol onto a silicon wafer (5 mm × 5 mm, previously washed in water/acetone). XPS measurements were performed at room temperature with a SPECS PHOIBOS 150 hemispherical analyzer (SPECS GmbH, Berlin, Germany) in a base pressure of 5 × 10^{-10} mbar using monochromatic Al K_{alpha} radiation (1486.74 eV) as excitation source. High resolution spectra of C1s, O1s, N1s and I3d regions were also registered.

2.3. Computer modelling of LiI@CNCs

Semiempirical quantum chemical calculations were used to explore the molecular structure and energetics of LiI adsorbed and encapsulated in nanocarbon materials. The xtb-GFN1 method [41], previously used to explain graphene-inorganic interfaces [42], was used within the periodic DFTB+ 22.1 software [43]. The LiI@graphene and LiI@CNT interfaces were built and modified with the aid of Virtual NanoLab [44] and the Atomic Simulation Environment (ASE) [45]. A (38,0) semiconducting single wall carbon nanotube was selected to represent LiI encapsulation. To compute the relative Li at. %, semiconducting MWCNTs were built by repeatedly adding CNTs with a 3.52 Å larger radius [46]. 3D periodic cells with 50 nm and 10 nm perpendicular axis to the molecular directions, i.e. layer and axis, were used to simulate the 2D and 1D systems respectively. The periodic cells used fixed slab and axis dimensions of 3.33 nm and 3 nm for graphene and the CNT respectively and were computed at the Γ point.

2.4. Internalization studies by confocal microscopy

To evaluate CNHs internalization in HeLa cells, $EuCl_3$@CNH were employed because europium allows their direct detection in confocal microscopy by light reflection. HeLa cells were selected as they represent a highly used *in vitro* model that it is proven to be useful as a starting point for research. A large amount of information is available about their properties and growing conditions.

To prepare the samples, sterile 20 mm × 20 mm coverslips were put inside 35 mm dish and 3 × 10^{4} cells were seeded on them. $EuCl_3$@CNHs were sterilized under UV light for 1 h and then dispersed in culture medium and ultrasonicated obtaining a concentration of 0.02 mg·mL^{-1}. Cells were allowed to grow for 24 h at 37 °C and 5% of CO_2, and then 1 mL of $EuCl_3$@CNHs solution was added to each dish without removing the previous millilitre obtaining a final concentration of 0.01 mg·mL^{-1}. Cells were incubated with CNHs for 24 h; after the contact time, medium was removed and cells were washed with DPBS (Dulbecco's phosphate buffered saline: 200 mg·mL^{-1} KCl, 200 mg·mL^{-1} KH_2PO_4, 8000 mg·mL^{-1} NaCl and 2160 mg·mL^{-1} Na_2HPO_4–$7H_2O$; ThermoFisher Scientific). Then, cells were fixed with paraformaldehyde (PFA) 4% for 20 min and washed with DPBS. Once they were fixed, HeLa cells were stained with Hoechst 33342 10 mg·mL^{-1} (InvitrogenTM), which stains the nuclear DNA, and Cell Mask Deep Red Membrane 5 mg·mL^{-1} (InvitrogenTM), which stains the plasma membrane. Dye dilutions in DPBS (1:1000) were prepared and 1 mL of them was added to the cells, they were incubated for 10 min at room temperature and shielded from light before being washed with DPBS, staining first the membrane and then the nucleus. After the staining, coverslips were transferred to glass slide using mounting media prolong glass to attach them; they were kept in the fridge until they were analysed with the confocal microscope.

For the acquisition, Leica TCS SP5 (Servei de Microscòpia de la UAB)

was employed using HCX PL APO lambda blue 63x/1.4 OIL UV objective. Lasers used for image acquisition were HeNe 633 nm (10%) for Cell Mask Deep Red Membrane (detection range from 643 nm to 782 nm), Diode UV 405 nm (6%) for Hoechst 33342 (detection range from 413 nm to 478 nm) and Argon laser at 488 nm (20%) for europium reflection (detection range from 483 nm to 497 nm). Final images were processed using ImageJ software.

2.5. Neutron irradiation experiments

2.5.1. Sample preparation for neutron irradiation

Neutron irradiation experiments with ^{6}LiI@CNCs were performed using KBr pellets. The pellets were prepared by grinding 200 mg of KBr with 2 mg of ^{6}LiI@CNCs using an agate mortar and pestle. The resulting mixture was pressed (5 tons) using a mould pellet press die with a diameter of 1.0 cm. These pellets were prepared to study the presence and the uniformity of lithium in nanomaterials, by means of qualitative autoradiography (see below).

2.5.2. Cell preparation and treatment with ^{6}LiI@CNCs

To evaluate the uptake, a rat osteosarcoma UMR-106 cell line was employed, as extensive experience of BNCT has been acquired using this model [47]. Cells were cultured in medium composed by DMEM high glucose, 10% FCS and 1% gentamicine. Then seeded at the density of 3 $\times$ 10^{6} cells in two 75 cm^{2} flasks. After 48 h, the culture medium was replaced, and cells were allowed to grow for 4 h in the medium enriched with the ^{6}LiI@CNCs. The ^{6}LiI@CNCs contained in each vial (4 mg or 0.4 mg), were dispersed in 20 mL of culture medium hand shaked until dissolved and then ultrasonicated for 30 min, leading to final concentrations of 0.2 and 0.02 mg·mL^{-1}. Before adding the enriched cell culture medium to the cell culture flasks, the enriched medium was exposed to UV light for 15 min to avoid cell contamination. At the end of the fixed contact time, after the medium removal, the cells were washed five times in DPBS (Euroclone Cat n° ECB4004L), trypsinized and counted. Finally, four million cells were selected and centrifuged, forming a condensed cell pellet. The pellet was then deposited on a mylar disk and left drying.

2.5.3. Neutron autoradiography

Neutron autoradiography is based on the use of passive detectors sensitive to the charged particles radiation. In this work, we used rectangular polyallyldiglycol carbonate (PADC) CR39 films. Samples containing elements capturing neutrons and emitting charged particles are irradiated in contact with the detector. After irradiation, the detector is etched in a chemical solution that enlarges the latent tracks and makes them visible for microscopical analysis. Depending on the calibration of the technique (neutron fluence, etching parameters), it can be employed to obtain quantitative information on the element concentration in sample or qualitative imaging of its spatial distribution.

Quantitative neutron autoradiography was used to check the lithium uptake in cell samples and the presence of lithium in KBr pellets, by detecting α tracks produced in the thermal neutron capture reaction on ^{6}Li.

The dry cell samples on the mylar disks were irradiated two times in contact with CR39 in the thermal neutron column of the TRIGA MARK II nuclear reactor at Laboratorio Energia Nucleare Applicata (LENA) of the University of Pavia. For the first irradiation, samples were irradiated for 30 min at 2 kW reactor power, receiving a thermal neutron fluence of 1.9 $\pm$ 0.1 $\times$ 10^{10} cm^{-2}. This neutron autoradiography set-up can provide quantitative autoradiography analysis by counting tracks generated by the α particles in the CR39 detector using a LEICA MZ16A microscope [48]. The results are presented as a composition of 40 (8 $\times$ 5) sequential pictures. Each image has an area of 0.3 mm^{2} (0.632 mm $\times$ 0.474 mm), giving a total measured area of 12 mm^{2}, which is a representative portion of the entire sample.

Qualitative images were obtained both for cell samples and for KBr pellets with a second irradiation. KBr pellets were placed on mylar disks and irradiated in contact with the CR39 films in the same way as cell pellets. Cell samples were placed on another CR39 and irradiated in the same position for 2 h at 250 kW. The higher neutron fluence causes a higher track density on the detector, which constitutes a map of Li distribution in the samples [49]. Qualitative autoradiography results in a black and white picture, where the gray halo represents the region with lithium uptake. The whiter parts of the images are the ones with higher lithium concentration.

2.5.4. In vitro neutron irradiation experiments

NCT effects were studied using the same cell line described above. To evaluate the effect of neutron capture in lithium, four flasks were prepared: 2 serving as the control, without any treatment (non-enriched cells) and 2 where cells were exposed to the ^{6}LiI@CNCs (enriched cells). Rat osteosarcoma UMR-106 cells were cultured in medium composed by DMEM high glucose, 10% FCS and 1% gentamicine, then seeded at the density of 3 $\times$ 10^{6} cells in four 75 cm^{2} flasks. After 48 h, for two flasks, the culture medium was replaced and cells were allowed to grow for 4 h in the medium enriched with the carbon nanomaterials containing lithium, following the same procedure as described in Section 2.2.2. At the end of the contact time, cells were washed, and fresh medium was added to the flask. The same procedure was performed for the other two control flasks. Finally, a non-enriched and an enriched cell flask were irradiated in the thermal column of the TRIGA Mark II reactor for 11 min at 250 kW. The irradiation position is characterized by a thermal neutron flux of about 10^{10} cm^{-2} s^{-1} at 250 kW. Cell survival was evaluated by means of cloning assay, measuring the plating efficiency.

3. Results and discussion

3.1. Preparation of CNCs from MWCNTs and CNHs

Within this work, two different types of carbon nanostructures, namely MWCNTs (Fig. 1a) and CNHs (Fig. 1e) were explored as nanocarriers for the delivery of enriched ^{6}Li into cancer cells. We notice that the preparation of viable carbon nanomaterials for melt filling is dependent on the employed carbon nanostructure. In the case of MWCNTs, a two-step treatment was usually needed for the preparation of nanocapsules. The first step consists in an oxidizing protocol, which combines a mixture of H_2SO_4/HNO_3 and ultrasonication. Acid treatment is a simple and efficient approach that allows cutting MWCNTs, removes metal particles (catalyst employed for the growth of CNTs) and induces the formation of oxygen-containing functional groups along the CNTs surface [36]. With the aim to discard long CNTs or bundles that can still be present after the oxidative cutting, we took advantage of the water dispersibility of the acid treated MWCNTs to fractionate them by length via centrifugation (at 4000 and 20000 rpm). The precipitated material at the bottom of the centrifuge tube was discarded and the supernatant was collected. In this way, we could obtain purified open-ended and very short MWCNTs with a narrow length distribution (Fig. 1b).

Fig. S1 shows the length distribution of the acid cut MWCNTs after applying different centrifugation speeds, namely, 4000 and 20000 rpm. The length distribution was determined by measuring over 1000 specimens from SEM images. Statistical analysis reveals an average length distribution of 186.2 $\pm$ 81.9 and 144.3 $\pm$ 53.9 nm for the MWCNTs centrifuged at 4000 rpm (Figure S1 a) and b)) and 20000 rpm (Figure S1 c) and d)), respectively. Therefore, due to the small average size and narrow distribution, MWCNTs obtained at the highest centrifugation speed were employed in subsequent studies. It is important to notice that the obtained length distributions are within the range of improved biocompatibility for CNTs [50]. AFM imaging corroborates the very short length of MWCNTs observed by SEM and give an additional overview of the morphology of the samples (Fig. S2). Subsequently, short MWCNTs were thermally reduced in order to remove the oxygen-based functionalities introduced on their graphitic structure by

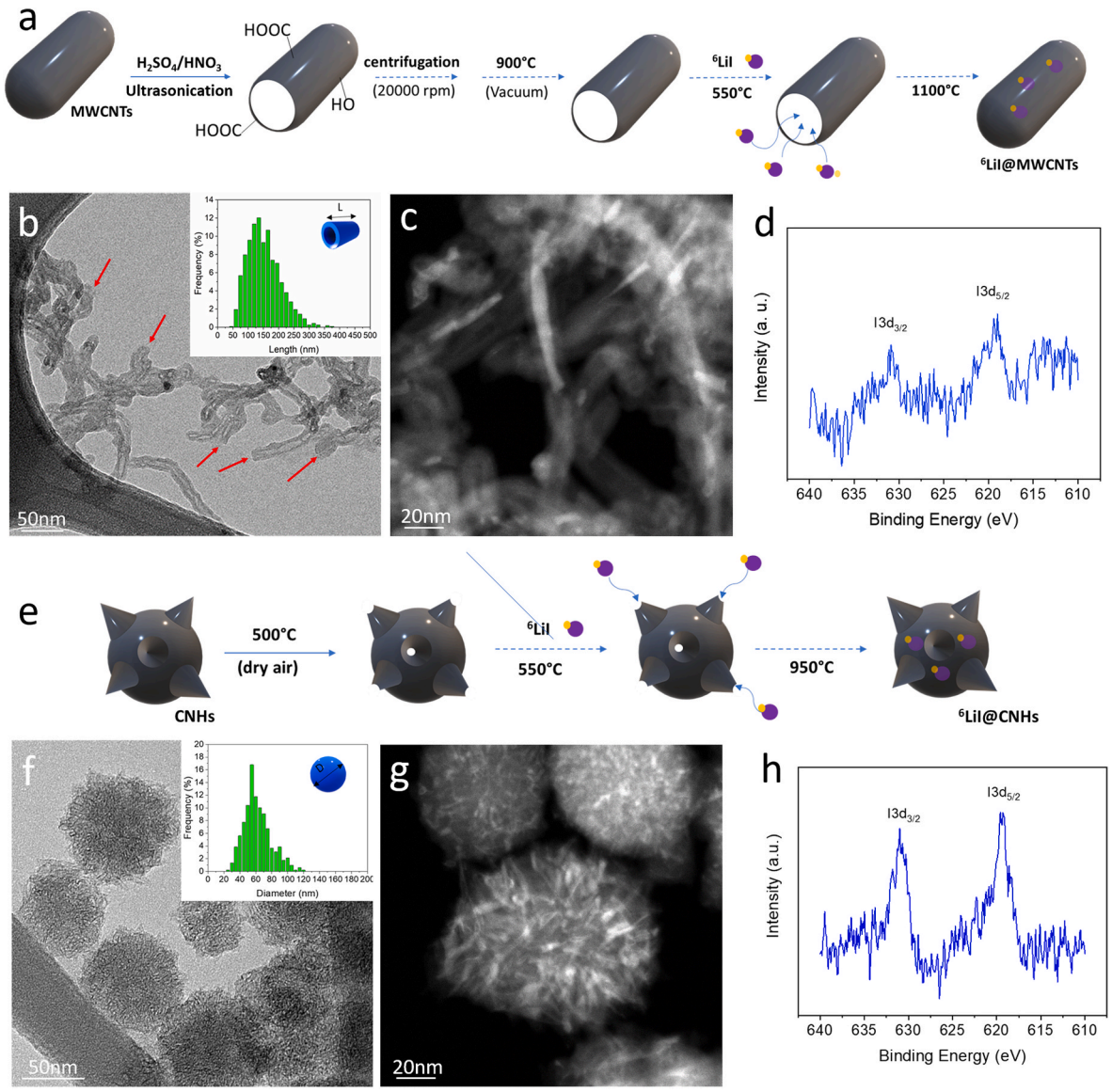

Fig. 1. Synthesis and characterization of carbon nanocapsules, short-MWCNTs and CNHs, filled with ^{6}LiI. a) Schematic representation of the synthesis of ^{6}LiI@MWCNTs. b) TEM image of the short-MWCNTs before filling with red arrows indicating the open tips; the inset shows the size distribution determined by SEM. c) HAADF STEM image of ^{6}LiI@MWCNTs showing high contrast of I (corresponding to ^{6}LiI) in the inner cavity of short-MWCNTs. d) HR-XPS spectrum of I3d corresponding to ^{6}LiI@MWCNTs. e) Schematic representation of the synthesis of ^{6}LiI@CNHs. f) TEM image of the CNHs before filling, with the inset showing the diameter distribution determined by SEM. g) HAADF STEM image of the ^{6}LiI@MWCNTs showing homogeneously distributed high contrast of I (from ^{6}LiI) in the inner cavities of CNHs. h) HR-XPS spectrum of I3d from ^{6}LiI@MWCNTs.

the acid treatment. The elimination of the aliphatic fractions was confirmed by thermogravimetric analysis (TGA, Fig. S3). Whereas the TGA curve of the acid treated MWCNTs shows a continuous weight loss due to the removal of adsorbed water and functional groups (red line), the vacuum annealed sample becomes thermally stable until its complete combustion at *ca.* 550 °C (green line).

The preparation CNHs suitable for the synthesis of CNCs is simpler and only requires a single oxidizing step for the controlled tip hole opening of their carbon structures (Fig. 1e) [37]. This controlled thermal oxidation can be applied because disruption of CNHs preferentially occurs through the tips, where a high density of structural defects or high strain is commonly present. As received CNHs were independently treated at 400 °C and 500 °C in air. The collected samples were analysed by BET to determine the specific surface area (SA), which allows estimating the degree of tip opening at each treatment temperature. Comparison of the SA of raw CNHs (CNHs = 419 $m^2 \cdot g^{-1}$) and after being annealed at 400 °C ($CNHs_{400°C}$ = 1317 $m^2 \cdot g^{-1}$) and 500 °C ($CNHs_{500°C}$ = 1857 $m^2 \cdot g^{-1}$) reveals the impact that temperature has on the degree of tip opening (Fig. S4). The largest surface area is reached at the highest employed temperature. The value of SA achieved for $CNHs_{500°C}$ is significantly higher than that reported by Fan et al. (1450 $m^2 \cdot g^{-1}$). It almost reaches the value achieved for graphene [51], showing that both sides of the single carbon layer in CNHs are fully accessible [37]. Additional characterization using TGA, under flowing air, reveals that both thermally treated CNHs present a similar combustion curve to as-received CNHs (Fig. S5). This indicates that the controlled oxidation at 400 °C and 500 °C takes only place in the tips and preserves the structural integrity of CNHs. Consequently, the CNHs with highest SA were selected for the development of nanocapsules. By having a large number of opened tips, it is expected to maximize the filling rate with the lithium compounds.

Fig. 1f shows a TEM image of CNHs after the oxidizing thermal

treatment at 500 °C. Statistical analysis reveals a median diameter of 59.3 ± 16.9 nm (inset Fig. 1f) determined by measuring over 500 specimens from SEM images. AFM and SEM images of CNHs are shown in Fig. S2 and Fig. S6.

3.2. Encapsulation of ^{6}Li onto CNCs (^{6}LiI@CNCs)

To maximize the lithium loading in short MWCNTs, via molten phase capillary wetting, several lithium salts were attempted, namely lithium iodide, lithium chloride and lithium fluoride. These salts were independently ground with a given amount of MWCNTs and sealed under vacuum in a silica ampoule. The mixture was then heated above the melting temperature of the salt to allow capillary wetting of the inner cavities of the open-ended MWCNTs by the molten halide. The obtained results showed that the high reactivity of lithium chloride and lithium fluoride with the silica ampoules at the temperatures employed for the filling step restrict their use in this approach (Fig. S7). Consequently, only lithium iodide (^{6}LiI) was explored on this work for the preparation of CNCs. In general, bulk filling of carbon nanomaterials results in the presence of a large amount of non-encapsulated compounds [52]. Therefore, after the filling experiment, ^{6}LiI that remained external to the MWCNTs or CNHs was removed from the sample by extensive washings in water (LiI solubility = 1.67 g·mL^{-1} at 25 °C).

The successful filling of MWCNTs and CNHs with ^{6}LiI was initially determined by Z-contrast imaging. Imaging of the encapsulated compound by Z-contrast STEM was possible because a large contrast is observed between I (Z = 53) and C (Z = 6) as a result of the Rutherford scattering used to form Z-contrast images, which scales approximately with the square of the atomic number [53,54]. This imaging modality has been widely employed to determine the crystal structure of inorganic compounds [55,56]. In the presence case, iodide atoms, from ^{6}LiI, are expected to appear much brighter than carbon. On the other hand, lithium, with a Z = 3, cannot be observed in this imaging modality. The presence of bright fragments inside the darker carbon shells confirms the successful loading of ^{6}LiI in the inner cavities of MWCNTs and CNHs (Fig. 1c and g, respectively, and Fig. S8). Moreover, bright particles were not observed external to the walls of the CNCs, confirming the full removal of the excess of ^{6}LiI employed in the synthesis. The selective dissolution of free ^{6}LiI while preserving the encapsulated material, of the same nature, indicates that the ends/tips of the carbon nanomaterials became closed during the filling experiment. This hermetically sealed carbon system isolates the encapsulated compound from the external medium, which is an essential aspect for the development of CNCs for biomedical purposes. It has been previously reported that the ends of MWCNTs can be sealed by thermal annealing, provided when a high enough temperature is given to the system [39]. Here we also provide evidence that the tips of CNHs are also able to be regenerated by adequate thermal treatment. Thermal regeneration of the ends of carbon nanostructures depends on their diameter. A higher temperature is for instance needed to seal multi-walled CNTs compared to their single-walled counterparts [39,57,58]. In the case of short-MWCNTs we employed 1100 °C, whereas in the case of CNHs we used 950 °C to promote simultaneously the process of filling and end closing.

Energy dispersive X-ray analysis (EDX) was next carried out to confirm the presence of I and for the semi-quantitative determination of the atomic composition of the synthesized materials. An estimated concentration of 0.25 at. % I and 0.63 at. % I was determined for ^{6}LiI@MWCNTs and ^{6}LiI@CNHs, respectively (Figs. S9–S10) indicating a higher metal halide loading in CNHs than in MWCNTs. X-ray photoelectron spectroscopy (XPS) data also confirm the presence of I (from ^{6}LiI) filled into both MWCNTs and CNHs cavities, with signals at *ca.* 620 eV corresponding to I3d (Fig. S11). The signal intensity of lithium was too low to be measurable by this technique. Therefore, the concentration of enriched lithium was determined based on the quantification of iodine in the I3d$_{5/2}$ high-resolution spectrum (Table S1). Considering that I and Li are equimolar (1:1 ratio), the atomic percentage of ^{6}Li in the sample turns out to be 1.4 at. % for ^{6}LiI@MWCNTs and 3.5 at. % for ^{6}LiI@CNHs (Table S1), corroborating the higher loading of the CNHs cavities with respect to MWCNTs already shown by EDX.

The successful formation of hermetically sealed nanostructures with ^{6}LiI nanometric crystals in the interior of MWCNTs and CNHs was confirmed by HRTEM (Fig. 2). Furthermore, it is also possible to confirm through visual inspection that the graphitic ends of the MWCNTs and CNHs (yellow arrowed) are reconstructed, forming in this way the desired hermetically sealed carbon nanocapsules (see Fig. S12 for additional images). Through intensity profiles acquired on different crystals we could determine interplanar spacings of 3.5 Å and 3.0 Å. These are in good agreement with the (111) plane and (200) of cubic LiI (Fm-3m (225), ICSD), respectively, and computer models of encapsulated LiI (see below).

3.2.1. Computer modelling of LiI@CNCs

To get insight into the filling and interaction of LiI with the graphene layers of the CNCs, computer models of LiI encapsulated into and onto graphene sheets and inside CNTs were studied. First, we investigated the interface of an increased number of LiI (100) monolayers ranging from one to six on a graphene square surface 3.3 × 3.3 nm containing 418 carbon atoms. The binding energy of LiI on graphene increases monotonically with the number of layers and is mostly converged from four LiI layers with a binding energy of 28 meV per carbon atom (Fig. S13). This is equivalent to an energy for the graphene-LiI interface of 0.17 J·m^{-2}, which is roughly half the energy binding two graphene layers computed with the same model (0.30 J·m^{-2}). Next, to understand better encapsulation, we computed systems with four, five and six LiI monolayers between two graphene layers. These monolayers were found to be 2.3, 2.0 and 1.7 nm apart, respectively, from which a LiI interlayer distance of 3.00 Å can be easily derived, in good agreement with the experimental measurements.

In addition, an analysis of the binding energies of both systems (Fig. 3) reveals that the binding between LiI adsorbed and encapsulated on layered Csp^{2} materials are virtually equivalent for the studied systems.

The molecular structure and energetics of LiI encapsulated in a 3 nm wide CNT containing 1064 carbon atoms was also studied. Two systems were computed, namely a LiI nanowire and a monolayer of LiI coating the inner CNT wall (Fig. 3 and Fig. S14), yielding binding energies of 21 meV and 15 meV per carbon atom, respectively. This means that, if needed, the release of Li would be energetically more likely for the monolayered LiI than for fully filled-up systems. The relative atomic percentages of Li are 16 at. % and 9 at. % for the LiI nanowire and LiI monolayer respectively. However, these values depend on the number of CNT walls, and for instance, for a MWCNT with six walls, the atomic percentages of Li get reduced to 2 at. % and 1 at. % for the LiI nanowire and the monolayer of LiI respectively, which are in the range of the experimental quantification.

3.3. Cell internalization studies

Cell internalization of CNCs is necessary for their application in ^{6}LiNCT. Therefore, after having proved that both CNTs and CNHs can be successfully filled, cell internalization studies were performed using CNHs. We focused on CNHs because filled CNTs have been extensively studied for biomedical imaging and therapy [59]. For this purpose, LiI was replaced by $EuCl_3$ using exactly the same protocol for the preparation of the nanocapsules. $EuCl_3$@CNHs were used to evaluate internalization since europium can be visualized by confocal microscopy. HeLa cells were exposed to 0.01 mg·mL^{-1} of $EuCl_3$@CNHs for 24 h. Then, they were fixed and dyed with Cell Mask Deep Red Membrane to stain the cell membrane and Hoechst 33342 to stain the nucleus, allowing the definition of cellular compartment and the better interpretation of particles location. Due to the fixation of the cells before the staining, Cell Mask Deep Red Membrane dyed not only the membrane but also the

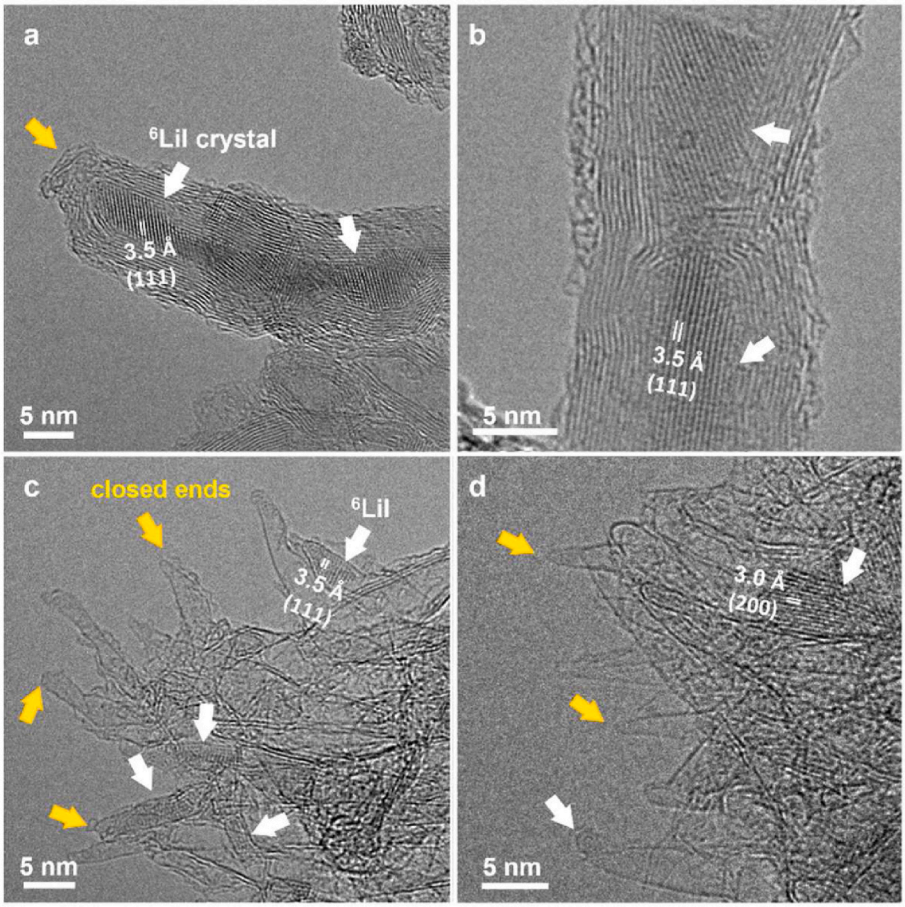

Fig. 2. Electron microscopy characterization of carbon nanocapsules. HRTEM images of a, b) ^{6}LiI@MWCNTs and c, d) ^{6}LiI@CNHs. Lattice fringes can be observed for several crystals of ^{6}LiI. As guide to the eye, white arrows point to encapsulated ^{6}LiI, and yellow arrows to closed ends.

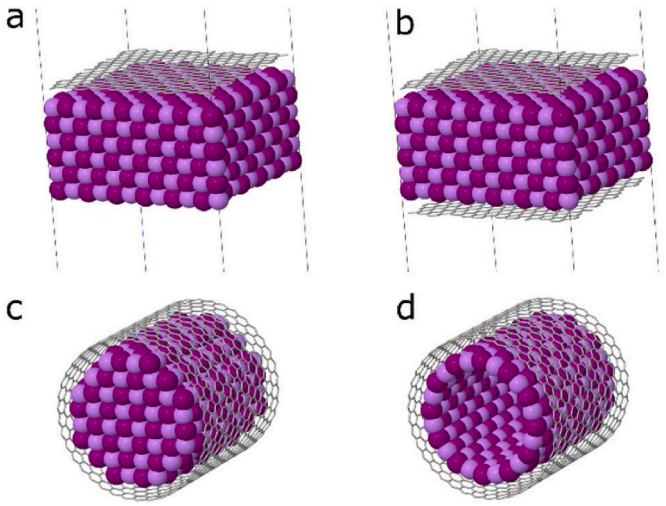

Fig. 3. Quantum chemical models of LiI@CNT, namely: a) six monolayers of LiI adsorbed on graphene, b) six monolayers of LiI encapsulated between two graphene sheets, c) LiI nanowire filling up a 3 nm wide CNT and d) LiI monolayer in a 3 nm wide CNT.

cytoplasm of the cells. Confocal images revealed the presence of the $EuCl_3$@CNHs (in green) inside HeLa cells. To precisely determine the location of $EuCl_3$@CNHs in the cells, orthogonal projections were performed. This allows the localization of the compounds in the three dimensions (x, y, z). Fig. 4 shows the orthogonal projections of two cells.

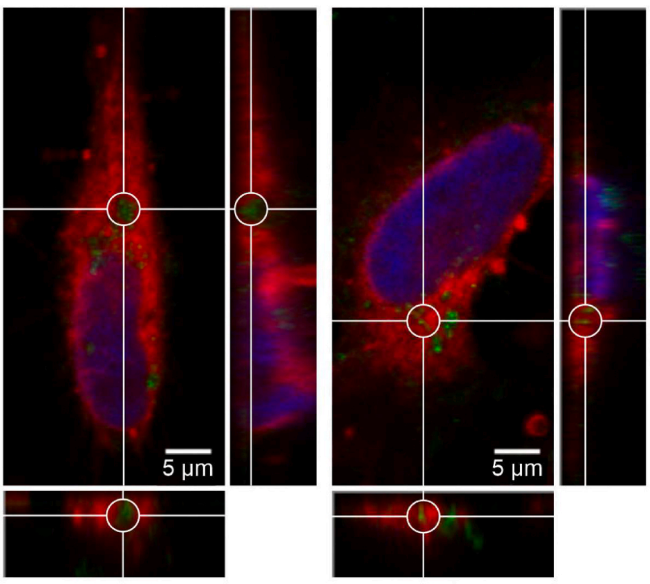

Fig. 4. Orthogonal projections of confocal images of HeLa cells incubated with 0.01 mg·mL^{-1} $EuCl_3$@CNHs in medium for 24 h. White lines determine the cut in each plane and the white circle indicates the position of some of the internalized $EuCl_3$@CNHs. $EuCl_3$@CNHs are shown in green, nucleus in blue and cytoplasm in red.

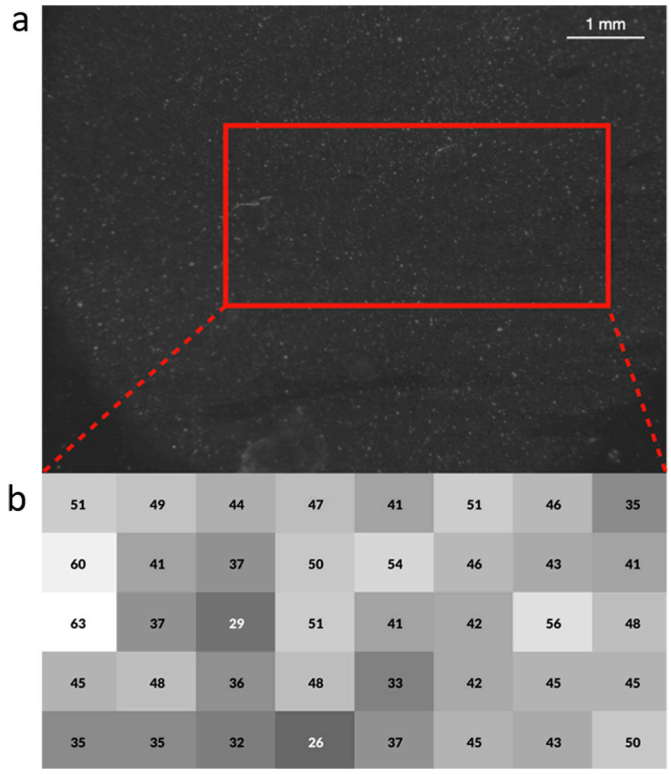

Fig. 5. a) Qualitative neutron autoradiography of the KBr pellet containing ^{6}LiI@MWCNTs. b). Quantitative distribution of lithium in a portion of the sample.

As a guide to the eye, some of the internalized $EuCl_3$@CNHs are marked with a white circle in each plane, showing their location inside the cytoplasm of HeLa cells. This analysis confirms internalization of the CNHs into the cells even at the low studied concentration of 0.01 mg·mL^{-1}.

3.4. Quantitative neutron autoradiography

To test whether the developed ^{6}LiI@CNCs held potential for LiNCT, an initial assessment was performed by neutron autoradiography using ^{6}LiI@MWCNTs dispersed in KBr pellets. ^{6}LiI@MWCNTs were chosen for these initial measurements because they have a lower content of ^{6}Li than ^{6}LiI@CNHs. Therefore, if ^{6}Li nuclei reacting with neutrons are already detected, the same would be expected for ^{6}LiI@CNHs. Fig. 5 shows the imaging of lithium distribution in KBr pellets. In the upper part, the qualitative neutron autoradiography is reported. This analysis allows pointing out the presence of neutron-capture elements and to evaluate their distribution over the surface of the detector. In fact, it is possible to see a distribution of clear structures over the black background. These structures are the tracks left by charged particles produced by neutron capture in lithium, enlarged by means of chemical etching and illuminated by a microscopy light field. In Fig. 5b, the quantitative analysis of a portion of the upper imaging (Fig. 5a) has been reported. Quantitative analysis refers to the count of tracks in single frames taken with the microscope in the same sample but irradiated with lower fluence to obtain a track distribution without superpositions. Another CR39 film is employed for this analysis. Each box in the zoomed part of the figure reports the number of tracks counted in the frames. It is important to notice that tracks are distributed over the entire pellet. Since MWCNTs tend to aggregate in bundles and the KBr pellet was prepared by simple grinding, the distribution of tracks is inhomogeneous. The inhomogeneities are shown by the white dots, which are track clusters caused by aggregates of lithium atoms. The quantitative neutron autoradiography analysis resulted in 44 ± 8 tracks mm^{-2}, where the uncertainty is the standard deviation of the tracks computed over the 40 images. These analyses confirm the presence of active lithium species in the sample.

3.5. External surface functionalization of CNCs (NH_2_^{6}LiI@CNCs)

The external surface functionalization of the ^{6}LiI@CNCs was performed using diazonium-based arylation reaction in presence of [(N-Boc)aminomethyl]aniline [40]. Fig. 6 a) shows a schematic representation of the included functional groups. After deprotection, the presence of ammonium groups on the external aromatic structure of the nanocarbon shelter confers good dispersibility in water and cell culture medium (Figs. S15 and S16) and it is expected to enhance its biocompatibility.

The composition of ^{6}LiI@CNC after chemical modification was determined by XPS analysis (Fig. 6 c and d). High resolution XPS spectra of the C1s, N1s and I3d were employed to quantitatively assess the concentration of C, N and I in the benzylamino functionalized samples. After considering the presence and stoichiometric ratio of both Li (from LiI) and H (present in the benzylamonium group), analyses reveal a similar relative atomic content of N1s for both ^{6}LiI@CNCs (1.9 at. %). The degree of functionalization was calculated taking into account the slights variations in C and I (the latter being higher in the case of NH_2_^{6}LiI@CNHs (1.0 at. % of I) than NH_2_^{6}LiI@MWCNTs (0.7 at. % of I)), the presence of H (7 H atoms per benzylamonium group containing moiety) and the equimolar concentration of I and ^{6}Li. This led to a surface chemical functionalization of 1.61 and 1.67 mmol·g^{-1} of CNHs and MWCNTs, respectively. These results indicate that the yield of the arylation for the covalent surface modification of the employed carbon nanostructures is barely affected by their morphology.

3.6. Biocompatibility and neutron autoradiography

Cytotoxicity studies of NH_2_^{6}LiI@CNCs were performed using UMR-106 cells, a well-known cell line in BNCT. Results showed that for both concentrations tested, namely 0.02 and 0.2 mg·mL^{-1}, the NH_2_^{6}LiI@MWCNT presented a lower cell viability, of about 75%, when compared with NH_2_^{6}LiI@CNHs that is >90% (Fig. 7a). The higher cytotoxicity of NH_2_^{6}LiI@MWCNT can be attributed to the morphology of the CNCs in this case, because cells are not in contact with the encapsulated ^{6}LiI, and the external functional groups are the same in both types of carbon nanostructures. Other groups have also compared these two types of nanocarbons. For instance, He et al. recently reported an improved biocompatibility of CNHs over four different types of CNTs in macrophages [60]. In fact, it is well known that the physico-chemical properties of nanomaterials, which can be tuned during their synthesis, determine their biological behaviour [61].

As the cell toxicity was acceptable, at least for one of the two formulations proposed, the next step consisted in studying the uptake of lithium in cells. When a cell is irradiated after the absorption of lithium, the neutron capture reaction releases charged particles that are responsible of the inactivation of the tumour cell itself, as shown in Fig. 7b. This same reaction is exploited by neutron autoradiography. The cell pellet previously treated with lithium-containing nanocapsules were irradiated in contact with the detectors, again applying the protocols of qualitative and quantitative autoradiography. Fig. 8a and b shows the qualitative neutron autoradiography of the ^{6}Li@CNC respectively produced by MWCNTs and CNHs, where the distribution of nanotubes is again represented by the white structures visible over the black background. The image in Fig. 8a shows that the distribution of nanoparticle produced via MWCNT inside cells is not uniform: they are concentrated in fact in two areas, while the large majority of the cell pellets does not evidence presence of lithium. This inhomogeneity may reflect a poor dispersibility of the compound in the cell culture medium and consequently a limited or no availability of lithium for the majority of the cells

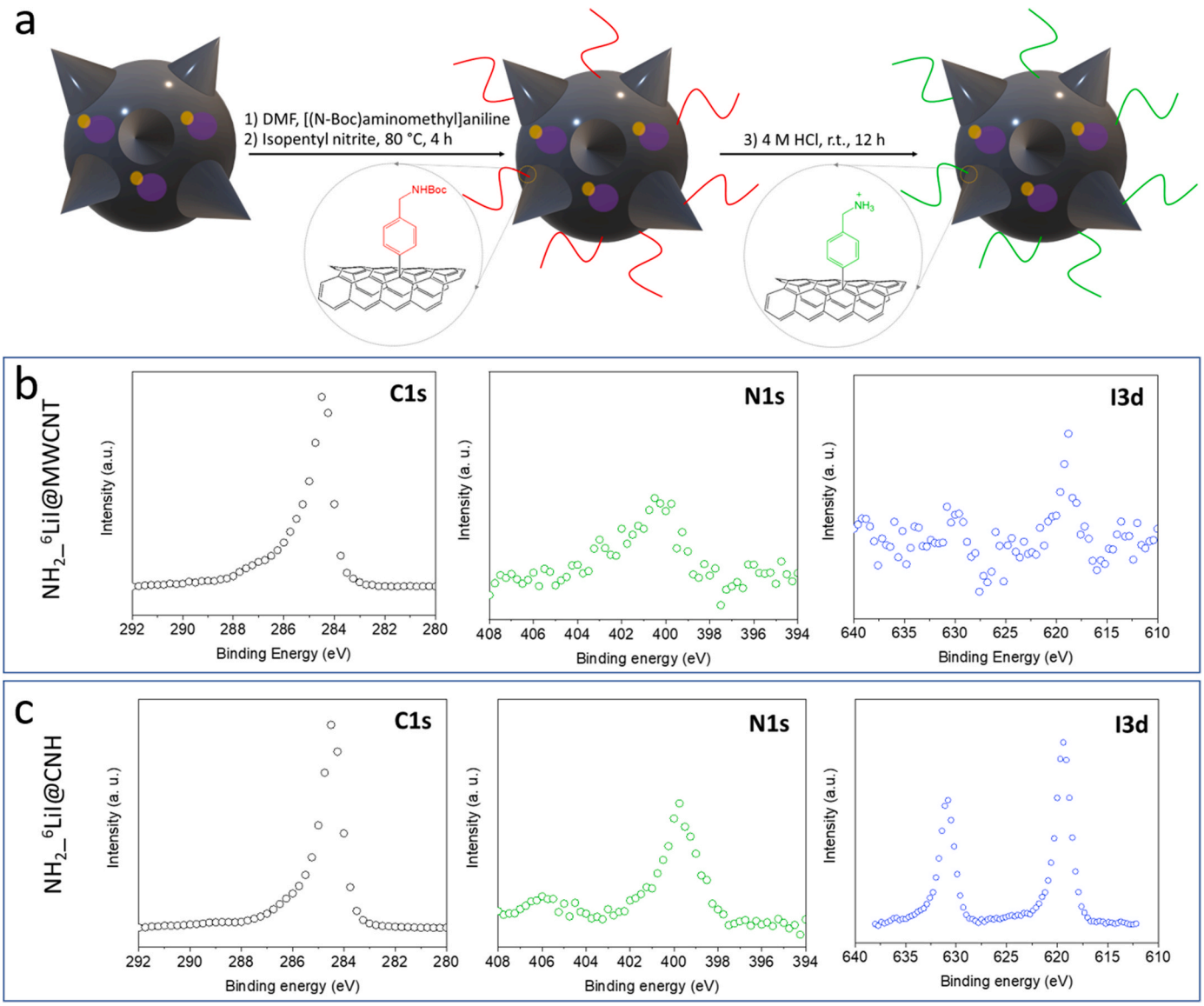

Fig. 6. a) Schematic representation of the chemical surface modification of ^{6}LiI@CNHs using diazonium-based arylation reaction in presence of [(N-Boc) aminomethyl]aniline. b, c) High-resolution XPS spectra over C1s, N1s and I3d for functionalized CNCs.

in the flask. This result suggests that this production route is not optimal for LiNCT: if only part of the tumour cells absorbs lithium, neutron irradiation would generate a non-uniform dose deposition and portion of tumour may survive. On the other hand, lithium enriched nanoparticles produced by CNH absorb lithium more homogeneously, as demonstrated by Fig. 8b. In this image, the white structures are evenly distributed on the surface of the pellet, corresponding to a uniform lithium concentration in cells. This is also confirmed by the quantitative analysis, resulting in an average track density of 23 ± 5 mm^{-2}. The uncertainty associated to this measure is the poissonian error of the counted tracks, reflecting the track distribution in the sample: a low relative uncertainty means that track density is very regular and does not fluctuate much between one frame (0.3 mm^2 image) to another. Therefore, the ^{6}LiI@CNCs based on CNHs hold higher potential for LiNCT as they would guarantee the deposition of a uniform dose in the tumour. See Figs. S17 and S18 for additional images.

3.7. *In vitro neutron irradiation experiments*

The NH_2_^{6}LiI@CNCs were used for a preliminary measurement of cell (Rat osteosarcoma UMR-106 cells) survival curves with plating efficiency after neutron irradiation; results are shown in Table 1. When the cells are not irradiated but are enriched with lithium, the cell survival is 92%, confirming the preliminary results obtained in the described experiments of biocompatibility. When cells are irradiated without lithium treatment, the survival drops at 4.2%, mainly due to neutron interaction with hydrogen and nitrogen in cells (background dose). When cells are irradiated after treatment with NH_2_^{6}LiI@CNHs, the survival is halved (1.8%) due to effect of neutron interaction with lithium. Being an initial test, a high neutron fluence was employed to increase the chances of observing an effect. Under the present dose conditions, it was observed a cell survival of 4.2%, that is consistent with previously reported results [47]. For lithium-treated cells, irradiated with the same fluence, a remarkable reduction in cell survival of more than 50% was achieved when compared with untreated ones (Table 1).

With the present approach the encapsulated ^{6}Li remains inactive until it is activated by an external neutron irradiation. This allows for the nanocapsules to be internalized by cells or even to be delivered to the diseased tissue *in vivo* with no biological effect (the latter being outside the scope of the present study). Only when the nanocapsules are located into the targeted site, they would be irradiated with external neutrons and emit lethal products, thus behaving as carbon nuclear nanobombs

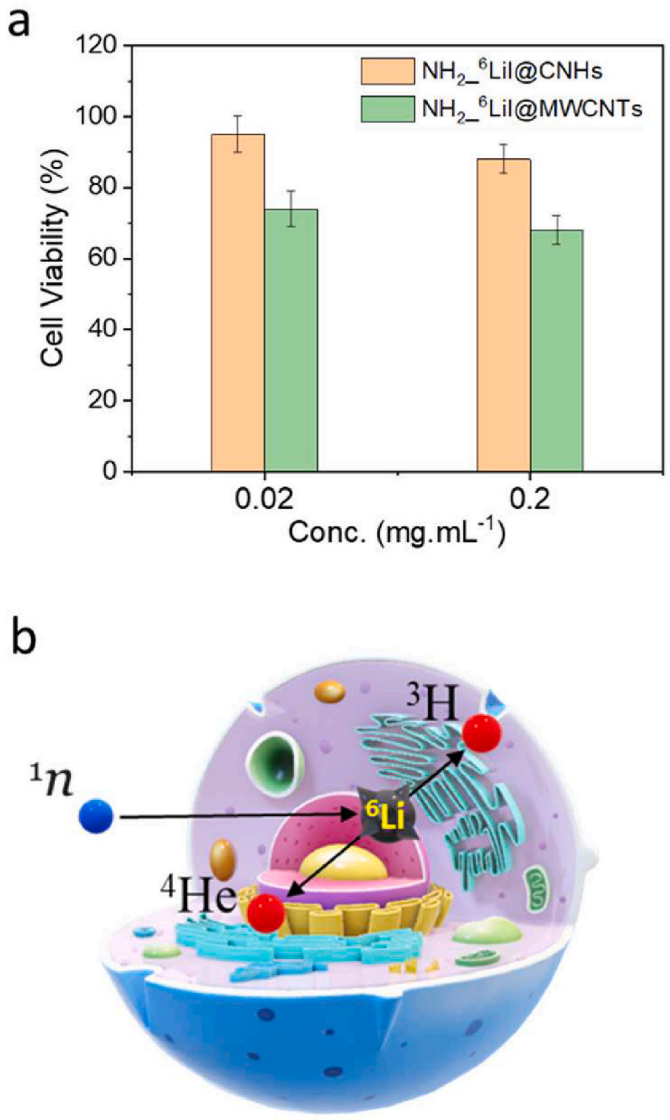

Fig. 7. Biocompatibility and neutron autoradiography studies of the developed nanocapsules with UMR-106 cells. a) Cytotoxicity studies of NH_2_^{6}LiI@CNCs with UMR-106 cells. b) Schematic representation of neutron irradiation of NH_2_^{6}LiI@CNCs inside of cell, and respective formation of nuclear species that can promote cell death.

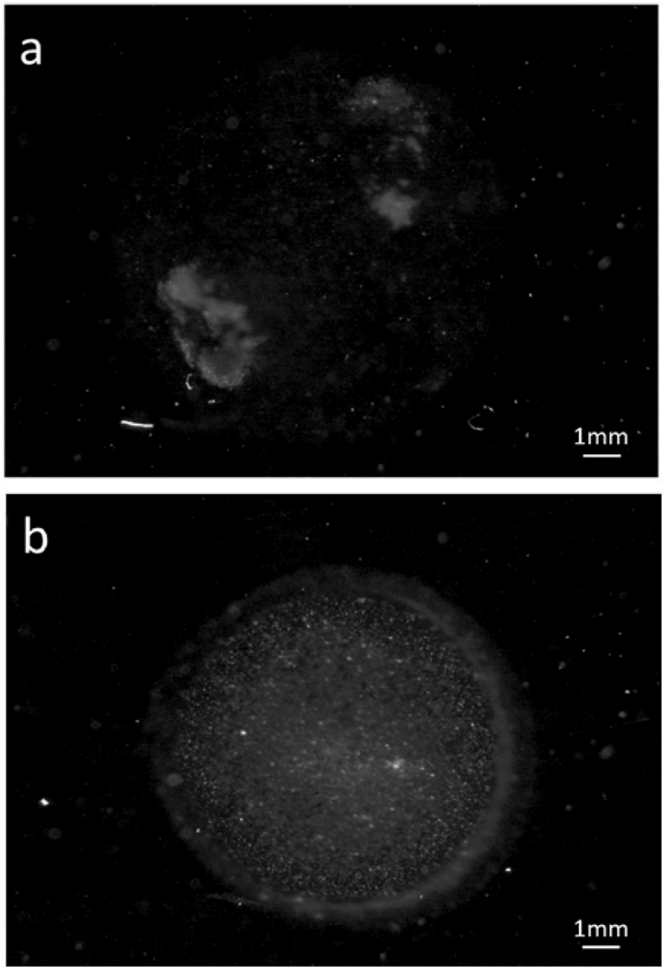

Fig. 8. Qualitative neutron autoradiography of a cell pellet exposed to a) NH_2_^{6}LiI@ MWCNTs and to b) NH_2_^{6}LiI@ CNHs at a concentration of 0.2 mg·mL^{-1}.

Table 1
Cell survival results obtained by plating efficiency.

Li enriched	Irradiated	Cell Survival (%)
✗	✗	100 ± 10
✓	✗	92 ± 12
✗	✓	4.2 ± 0.3
✓	✓	1.8 ± 0.3

(CNBs). Next steps for the implementation of LiNCT include *in vitro* neutron dose optimization, a higher encapsulation efficiency of ^{6}Li and the use of targeted nanocapsules for the selective accumulation of ^{6}Li at the tumor site.

4. Conclusions

We have successfully developed new CNCs for the containment of ^{6}LiI using both CNHs and MWCNTs. With neutron autoradiography we have shown that ^{6}Li can be efficiently internalized by UMR cells. The accumulation of ^{6}Li in the cells is more homogeneous when using NH_2_^{6}LiI@CNCs produced with CNHs compared to that produced with MWCNTs. In fact, in the first case the concentration of ^{6}Li present in the cells produced an average spatial track density of 23 ± 5 mm^{-2} in the CR39, while in the second case this was very inhomogeneous. In addition, the NH_2_^{6}LiI@CNHs demonstrated low toxicity at the cellular level. A first preliminary test of thermal neutron irradiation of UMR cells treated with NH_2_^{6}LiI@CNHs showed that, with the concentration of 0.2 mg·mL^{-1}, the survival of the cells is reduced compared to an irradiation without ^{6}Li. In addition, the NH_2_^{6}LiI@CNHs demonstrated low toxicity at the cellular level in absence of irradiation. These results give a first indication of the possibility of using these CNCs for LiNCT and encourage us to plan a systematic study to estimate the dose in cells due to the reaction, with the aim to produce a complete cell survival curve. This will allow to evaluate the effective therapeutic potential of the developed lithium-filled nanocapsules. The present study expands the potentialities that LiNCT holds for the treatment of cancer.

Declaration of competing interest

The authors declare the following financial interests/personal

relationships which may be considered as potential competing interests: priority patent application entitled "Lithium filled nanocapsules and use thereof", P202230271.

Acknowledgements

G. T. acknowledges funding from ERC Consolidator Grant NEST (725743). G.G. gratefully acknowledges the funding by the Portuguese Science Foundation (FCT) for Programme Stimulus of Scientific Employment – Individual Support (CEECIND/01913/2017), financial support of project CARBONCT (2022.03596.PTDC), TEMA UIDB/00481/2020 and UIDP/00481/2020; and CENTRO-01-0145-FEDER-022083 - Centro Portugal Regional Operational Programme (Centro2020), under the PORTUGAL 2020 Partnership Agreement, through the European Regional Development Fund. In addition, support through the project IF/00894/2015 and within the scope of the project CICECO-Aveiro Institute of Materials, UIDB/50011/2020, UIDP/50011/2020 & LA/P/0006/2020, financed by national funds through the FCT/MEC (PIDDAC) is gratefully acknowledged. We acknowledge funding by INFN (CSN5)-project ENTER_BNCT. ICMAB and ICN2 acknowledge financial support from the Spanish Ministry of Economy and Competitiveness (Spain), through the "Severo Ochoa" Programme for Centres of Excellence in R&D (CEX2019-000917-S and CEX2021-001214-S respectively). ICN2 is supported by CERCA programme. We acknowledge funding from Generalitat de Catalunya (2021-SGR-00439, 2017 SGR 327). M.Ll. has carried out this work in the framework of the Doctoral Degree Program in Materials Science of the Universitat Autònoma de Barcelona. We acknowledge fruitful discussions with Manuel Altabas and support with the XPS analysis by Guillaume Sauthier.

Appendix A. Supplementary data

Supplementary data to this article can be found online at https://doi.org/10.1016/j.carbon.2023.03.034.

References

[1] A. Curt, H.J.A. Van Hedel, D. Klaus, V. Dietz, Recovery from a spinal cord injury: significance of compensation, neural plasticity, and repair, J. Neurotrauma 25 (2008) 677–685, https://doi.org/10.1089/neu.2007.0468.
[2] M. Suzuki, Boron neutron capture therapy (BNCT): a unique role in radiotherapy with a view to entering the accelerator-based BNCT era, Int. J. Clin. Oncol. 25 (2020) 43–50, https://doi.org/10.1007/s10147-019-01480-4.
[3] K. Hirose, A. Konno, S. Yoshimoto, K. Ono, N. Otsuki, J. Hatazawa, J. Hiratsuka, Y. Takai, A prospective phase 2 trial of accelerator-based boron neutron capture therapy for recurrent and locally advanced head and neck cancer: initial report of treatment outcome, Int. J. Radiat. Oncol. 105 (2019) E374, https://doi.org/10.1016/j.ijrobp.2019.06.1625.
[4] R.F. Barth, Z. Zhang, T. Liu, A realistic appraisal of boron neutron capture therapy as a cancer treatment modality, Cancer Commun. 38 (2018) 36, https://doi.org/10.1186/s40880-018-0280-5.
[5] T.-Z. Yuan, S.-Q. Xie, C.-N. Qian, Boron neutron capture therapy of cancer: critical issues and future prospects, Thorac. Cancer. 10 (2019) 2195–2199, https://doi.org/10.1111/1759-7714.13232.
[6] N.V. Gubanova, A.R. Tsygankova, E.L. Zavjalov, A.V. Romashchenko, Y.L. Orlov, Biodistribution of 10B in glioma orthotopic xenograft mouse model after injection of L-para-boronophenylalanine and sodium borocaptate, Biomedicines 9 (2021) 722, https://doi.org/10.3390/biomedicines9070722.
[7] R.F. Barth, P. Mi, W. Yang, Boron delivery agents for neutron capture therapy of cancer, Cancer Commun. 38 (2018) 35, https://doi.org/10.1186/s40880-018-0299-7. London, England.
[8] C. Viñas, R. Núñez, I. Bennour, F. Teixidor, Periphery decorated and core initiated neutral and polyanionic borane large molecules: forthcoming and promising properties for medicinal applications, Curr. Med. Chem. 26 (2019) 5036–5076, https://doi.org/10.2174/0929867326666190603123838.
[9] M. Nuez-Martinez, C.I.G. Pinto, J.F. Guerreiro, F. Mendes, F. Marques, A. Muñoz-Juan, J.A. Xavier, A. Laromaine, V. Bitonto, N. Protti, S.G. Crich, F. Teixidor, C. Viñas, Cobaltabis(dicarbollide) ([o-COSAN]−) as multifunctional chemotherapeutics: a prospective application in boron neutron capture therapy (BNCT) for glioblastoma,, Cancers 13 (2021), https://doi.org/10.3390/cancers13246367.
[10] S.N. Bhatia, X. Chen, M.A. Dobrovolskaia, T. Lammers, Cancer nanomedicine, Nat. Rev. Cancer 22 (2022) 550–556, https://doi.org/10.1038/s41568-022-00496-9.
[11] K. Hu, Z. Yang, L. Zhang, L. Xie, L. Wang, H. Xu, L. Josephson, S.H. Liang, M.-R. Zhang, Boron agents for neutron capture therapy, Coord. Chem. Rev. 405 (2020), 213139, https://doi.org/10.1016/j.ccr.2019.213139.
[12] D. Alberti, A. Deagostino, A. Toppino, N. Protti, S. Bortolussi, S. Altieri, S. Aime, S. Geninatti Crich, An innovative therapeutic approach for malignant mesothelioma treatment based on the use of Gd/boron multimodal probes for MRI guided BNCT, J. Control. Release Off. J. Control. Release Soc. 280 (2018) 31–38, https://doi.org/10.1016/j.jconrel.2018.04.043.
[13] K.R. Pulagam, M. Henriksen-Lacey, K.B. Uribe, C. Renero-Lecuna, J. Kumar, A. Charalampopoulou, A. Facoetti, N. Protti, V. Gómez-Vallejo, Z. Baz, V. Kumar, A. Sánchez-Iglesias, S. Altieri, U. Cossío, D. Di Silvio, A.M. Martínez-Villacorta, A. Ruiz de Angulo, L. Rejc, L.M. Liz-Marzán, J. Llop, In vivo evaluation of multifunctional gold nanorods for boron neutron capture and photothermal therapies, ACS Appl. Mater. Interfaces 13 (2021) 49589–49601, https://doi.org/10.1021/acsami.0c17575.
[14] T.V. Popova, I.A. Pyshnaya, O.D. Zakharova, A.E. Akulov, O.B. Shevelev, J. Poletaeva, E.L. Zavjalov, V.N. Silnikov, E.I. Ryabchikova, T.S. Godovikova, Rational design of albumin theranostic conjugates for gold nanoparticles anticancer drugs: where the seed meets the soil? Biomedicines 9 (2021) 74, https://doi.org/10.3390/biomedicines9010074.
[15] A.H. Soloway, W. Tjarks, B.A. Barnum, F.-G. Rong, R.F. Barth, I.M. Codogni, J. G. Wilson, The chemistry of neutron capture therapy, Chem. Rev. 98 (1998) 1515–1562, https://doi.org/10.1021/cr941195u.
[16] P.A. Zahl, F.S. Cooper, J.R. Dunning, Some in vivo effects of localized nuclear disintegration products on a transplantable mouse sarcoma, Proc. Natl. Acad. Sci. United States Am. 26 (1940) 589–598, https://doi.org/10.1073/pnas.26.10.589.
[17] P.A. Zahl, F.S. Cooper, Physical and biological considerations in the use of slow neutrons for cancer therapy, Radiology 37 (1941) 673–682, https://doi.org/10.1148/37.6.673.
[18] P.A. Zahl, F.S. Cooper, Localization of lithium in tumor tissue as a basis for slow neutron therapy, Science 93 (1941) 64–65, https://doi.org/10.1126/science.93.2403.64.
[19] R. Núñez, M. Tarrés, A. Ferrer-Ugalde, F.F. de Biani, F. Teixidor, Electrochemistry and photoluminescence of icosahedral carboranes, boranes, metallacarboranes, and their derivatives, Chem. Rev. 116 (2016) 14307–14378, https://doi.org/10.1021/acs.chemrev.6b00198.
[20] D. Olid, R. Núñez, C. Viñas, F. Teixidor, Methods to produce B–C, B–P, B–N and B–S bonds in boron clusters, Chem. Soc. Rev. 42 (2013) 3318–3336, https://doi.org/10.1039/C2CS35441A.
[21] L.M. Rendina, Can lithium salts herald a new era for neutron capture therapy? J. Med. Chem. 53 (2010) 8224–8227, https://doi.org/10.1021/jm100836m.
[22] L. Tondo, M. Alda, M. Bauer, V. Bergink, P. Grof, T. Hajek, U. Lewitka, R.W. Licht, M. Manchia, B. Müller-Oerlinghausen, R.E. Nielsen, M. Selo, C. Simhandl, R. J. Baldessarini, For the I.G. for S. of L. (IGSLi), Clinical use of lithium salts: guide for users and prescribers, Int. J. Bipolar Disord. 7 (2019) 16, https://doi.org/10.1186/s40345-019-0151-2.
[23] D. Draaisma, Lithium: the gripping history of a psychiatric success story, Nature 572 (2019) 584–586.
[24] D. Li, Y. Zhang, J. Xu, F. Yoshino, H. Xu, X. Chen, L. Zhao, Surface-engineered carbon nanohorns as a theranostic nanodevice for photoacoustic imaging and effective radiochemotherapy of cancer, Carbon N. Y. 180 (2021) 185–196, https://doi.org/10.1016/j.carbon.2021.04.073.
[25] Y. Maeda, E. Hirata, Y. Takano, N. Sakaguchi, N. Ushijima, A. Saeki, S. Kimura, K. Shibata, M. Yudasaka, A. Yokoyama, Stable aqueous dispersions of carbon nanohorns loaded with minocycline and exhibiting antibacterial activity, Carbon N. Y. 166 (2020) 36–45, https://doi.org/10.1016/j.carbon.2020.04.040.
[26] S. Guo, Z. Song, D.-K. Ji, G. Reina, J.-D. Fauny, Y. Nishina, C. Ménard-Moyon, A. Bianco, Combined photothermal and photodynamic therapy for cancer treatment using a multifunctional graphene oxide, Pharmaceutics 14 (2022), https://doi.org/10.3390/pharmaceutics14071365.
[27] V. Meunier, C. Ania, A. Bianco, Y. Chen, G.B. Choi, Y.A. Kim, N. Koratkar, C. Liu, J. M.D. Tascon, M. Terrones, Carbon science perspective in 2022: current research and future challenges, Carbon N. Y. 195 (2022) 272–291, https://doi.org/10.1016/j.carbon.2022.04.015.
[28] S.I. Amaral, R. Costa-Almeida, I.C. Gonçalves, F.D. Magalhães, A.M. Pinto, Carbon nanomaterials for phototherapy of cancer and microbial infections, Carbon N. Y. 190 (2022) 194–244, https://doi.org/10.1016/j.carbon.2021.12.084.
[29] C.J. Serpell, K. Kostarelos, B.G. Davis, Can carbon nanotubes deliver on their promise in biology? Harnessing unique properties for unparalleled applications, ACS Cent. Sci. 2 (2016) 190–200, https://doi.org/10.1021/acscentsci.6b00005.
[30] S.Y. Hong, G. Tobias, K.T. Al-Jamal, B. Ballesteros, H. Ali-Boucetta, S. Lozano-Perez, P.D. Nellist, R.B. Sim, C. Finucane, S.J. Mather, M.L.H. Green, K. Kostarelos, B.G. Davis, Filled and glycosylated carbon nanotubes for in vivo radioemitter localization and imaging, Nat. Mater. 9 (2010) 485–490, https://doi.org/10.1038/nmat2766.
[31] H. Ge, P.J. Riss, V. Mirabello, D.G. Calatayud, S.E. Flower, R.L. Arrowsmith, T. D. Fryer, Y. Hong, S. Sawiak, R.M.J. Jacobs, S.W. Botchway, R.M. Tyrrell, T. D. James, J.S. Fossey, J.R. Dilworth, F.I. Aigbirhio, S.I. Pascu, Behavior of supramolecular assemblies of radiometal-filled and fluorescent carbon nanocapsules in vitro and in vivo, Chem 3 (2017) 437–460, https://doi.org/10.1016/j.chempr.2017.06.013.
[32] C.J. Serpell, R.N. Rutte, K. Geraki, E. Pach, M. Martincic, M. Kierkowicz, S. De Munari, K. Wals, R. Raj, B. Ballesteros, G. Tobias, D.C. Anthony, B.G. Davis, Carbon nanotubes allow capture of krypton, barium and lead for multichannel biological X-ray fluorescence imaging, Nat. Commun. 7 (2016), https://doi.org/10.1038/ncomms13118.

[33] J.T.-W. Wang, R. Klippstein, M. Martincic, E. Pach, R. Feldman, M. Šefl, Y. Michel, D. Asker, J.K. Sosabowski, M. Kalbac, T. Da Ros, C. Ménard-Moyon, A. Bianco, I. Kyriakou, D. Emfietzoglou, J.-C. Saccavini, B. Ballesteros, K.T. Al-Jamal, G. Tobias, Neutron activated ^{153}Sm sealed in carbon nanocapsules for in vivo imaging and tumor radiotherapy, ACS Nano 14 (2020), https://doi.org/10.1021/acsnano.9b04898.

[34] J.T.-W. Wang, C. Spinato, R. Klippstein, P.M. Costa, M. Martincic, E. Pach, A. P. Ruiz de Garibay, C. Ménard-Moyon, R. Feldman, Y. Michel, M. Šefl, I. Kyriakou, D. Emfietzoglou, J.-C. Saccavini, B. Ballesteros, G. Tobias, A. Bianco, K.T. Al-Jamal, Neutron-irradiated antibody-functionalised carbon nanocapsules for targeted cancer radiotherapy, Carbon N. Y. 162 (2020) 410–422, https://doi.org/10.1016/j.carbon.2020.02.060.

[35] A. Gajewska, J.T.-W. Wang, R. Klippstein, M. Martincic, E. Pach, R. Feldman, J.-C. Saccavini, G. Tobias, B. Ballesteros, K.T. Al-Jamal, T. Da Ros, Functionalization of filled radioactive multi-walled carbon nanocapsules by arylation reaction for in vivo delivery of radio-therapy, J. Mater. Chem. B. 10 (2022) 47–56, https://doi.org/10.1039/D1TB02195H.

[36] M. Kierkowicz, E. Pach, A. Santidrián, S. Sandoval, G. Gonçalves, E. Tobías-Rossell, M. Kalbáč, B. Ballesteros, G. Tobias, Comparative study of shortening and cutting strategies of single-walled and multi-walled carbon nanotubes assessed by scanning electron microscopy, Carbon N. Y. 139 (2018) 922–932, https://doi.org/10.1016/j.carbon.2018.06.021.

[37] S. Utsumi, J. Miyawaki, H. Tanaka, Y. Hattori, T. Itoi, N. Ichikuni, H. Kanoh, M. Yudasaka, S. Iijima, K. Kaneko, Opening mechanism of internal nanoporosity of single-wall carbon nanohorn, J. Phys. Chem. B 109 (2005) 14319–14324, https://doi.org/10.1021/jp0512661.

[38] G. Brown, S.R. Bailey, M. Novotny, R. Carter, E. Flahaut, K.S. Coleman, J. L. Hutchison, M.L.H. Green, J. Sloan, High yield incorporation and washing properties of halides incorporated into single walled carbon nanotubes, Appl. Phys. A 76 (2003) 457–462, https://doi.org/10.1007/s00339-002-2040-1.

[39] M. Martincic, S. Vranic, E. Pach, S. Sandoval, B. Ballesteros, K. Kostarelos, G. Tobias, Non-cytotoxic carbon nanocapsules synthesized via one-pot filling and end-closing of multi-walled carbon nanotubes, Carbon N. Y. 141 (2019) 782–793, https://doi.org/10.1016/j.carbon.2018.10.006.

[40] J.M. González-Domínguez, A. Santidrián, A. Criado, C. Hadad, M. Kalbáč, T. Da Ros, Multipurpose nature of rapid covalent functionalization on carbon nanotubes, Chem. Eur J. 21 (2015) 18631–18641, https://doi.org/10.1002/chem.201503085.

[41] S. Grimme, C. Bannwarth, P. Shushkov, A robust and accurate tight-binding quantum chemical method for structures, vibrational frequencies, and noncovalent interactions of large molecular systems parametrized for all spd-block elements (Z = 1–86), J. Chem. Theor. Comput. 13 (2017) 1989–2009, https://doi.org/10.1021/acs.jctc.7b00118.

[42] S. Piovesana, D. Iglesias, M. Melle-Franco, S. Kralj, C. Cavaliere, M. Melchionna, A. Laganà, A.L. Capriotti, S. Marchesan, Carbon nanostructure morphology templates nanocomposites for phosphoproteomics, Nano Res. 13 (2020) 380–388, https://doi.org/10.1007/s12274-020-2620-4.

[43] B. Hourahine, B. Aradi, V. Blum, F. Bonafé, A. Buccheri, C. Camacho, C. Cevallos, M.Y. Deshaye, T. Dumitricä, A. Dominguez, S. Ehlert, M. Elstner, T. van der Heide, J. Hermann, S. Irle, J.J. Kranz, C. Köhler, T. Kowalczyk, T. Kubař, I.S. Lee, V. Lutsker, R.J. Maurer, S.K. Min, I. Mitchell, C. Negre, T.A. Niehaus, A.M. N. Niklasson, A.J. Page, A. Pecchia, G. Penazzi, M.P. Persson, J. Řezáč, C. G. Sánchez, M. Sternberg, M. Stöhr, F. Stuckenberg, A. Tkatchenko, V.W. -z. Yu, T. Frauenheim, DFTB+, a software package for efficient approximate density functional theory based atomistic simulations, J. Chem. Phys. 152 (2020), 124101, https://doi.org/10.1063/1.5143190.

[44] D. Stradi, L. Jelver, S. Smidstrup, K. Stokbro, Method for determining optimal supercell representation of interfaces, J. Phys. Condens. Matter 29 (2017), 185901, https://doi.org/10.1088/1361-648x/aa66f3.

[45] A. Hjorth Larsen, J. Jørgen Mortensen, J. Blomqvist, I.E. Castelli, R. Christensen, M. Dułak, J. Friis, M.N. Groves, B. Hammer, C. Hargus, E.D. Hermes, P.C. Jennings, P. Bjerre Jensen, J. Kermode, J.R. Kitchin, E. Leonhard Kolsbjerg, J. Kubal, K. Kaasbjerg, S. Lysgaard, J. Bergmann Maronsson, T. Maxson, T. Olsen, L. Pastewka, A. Peterson, C. Rostgaard, J. Schiøtz, O. Schütt, M. Strange, K. S. Thygesen, T. Vegge, L. Vilhelmsen, M. Walter, Z. Zeng, K.W. Jacobsen, The atomic simulation environment—a Python library for working with atoms, J. Phys. Condens. Matter 29 (2017), 273002, https://doi.org/10.1088/1361-648x/aa680e.

[46] L. Bellarosa, E. Bakalis, M. Melle-Franco, F. Zerbetto, Interactions in concentric carbon nanotubes: the radius vs the chirality angle contributions, Nano Lett. 6 (2006) 1950–1954, https://doi.org/10.1021/nl061066g.

[47] S. Bortolussi, I. Postuma, N. Protti, L. Provenzano, C. Ferrari, L. Cansolino, P. Dionigi, O. Galasso, G. Gasparini, S. Altieri, S.-I. Miyatake, S.J. González, Understanding the potentiality of accelerator based-boron neutron capture therapy for osteosarcoma: dosimetry assessment based on the reported clinical experience, Radiat. Oncol. 12 (2017) 130, https://doi.org/10.1186/s13014-017-0860-6.

[48] I. Postuma, S. Bortolussi, N. Protti, F. Ballarini, P. Bruschi, L. Ciani, S. Ristori, L. Panza, C. Ferrari, L. Cansolino, S. Altieri, An improved neutron autoradiography set-up for (10)B concentration measurements in biological samples, Reports Pract. Oncol. Radiother. J. Gt. Cancer Cent. Pozn. Polish Soc. Radiat. Oncol. 21 (2016) 123–128, https://doi.org/10.1016/j.rpor.2015.10.006.

[49] S. Altieri, S. Bortolussi, P. Bruschi, P. Chiari, F. Fossati, S. Stella, U. Prati, L. Roveda, A. Zonta, C. Zonta, C. Ferrari, A. Clerici, R. Nano, T. Pinelli, Neutron autoradiography imaging of selective boron uptake in human metastatic tumours, Appl. Radiat. Isot. Incl. Data, Instrum. Methods Use Agric. Ind. Med. 66 (2008) 1850–1855, https://doi.org/10.1016/j.apradiso.2008.05.007.

[50] K. Kostarelos, The long and short of carbon nanotube toxicity, Nat. Biotechnol. 26 (2008) 774–776, https://doi.org/10.1038/nbt0708-774.

[51] A. Kovtun, E. Treossi, N. Mirotta, A. Scidà, A. Liscio, M. Christian, F. Valorosi, A. Boschi, R.J. Young, C. Galiotis, I.A. Kinloch, V. Morandi, V. Palermo, Benchmarking of graphene-based materials: real commercial products versus ideal graphene, 2D Mater. 6 (2019), 25006, https://doi.org/10.1088/2053-1583/aafc6e.

[52] M. Kierkowicz, J.M. González-Domínguez, E. Pach, S. Sandoval, B. Ballesteros, T. Da Ros, G. Tobias, Filling single-walled carbon nanotubes with lutetium chloride: a sustainable production of nanocapsules free of nonencapsulated material, ACS Sustain. Chem. Eng. 5 (2017) 2501–2508, https://doi.org/10.1021/acssuschemeng.6b02850.

[53] A.V. Crewe, J. Wall, J. Langmore, Visibility of single atoms, Science 168 (1970) 1338–1340, https://doi.org/10.1126/science.168.3937.1338.

[54] P.D. Nellist, S.J. Pennycook, Science 274 (1996) 413.

[55] R.J. Kashtiban, C.E. Patrick, Q. Ramasse, R.I. Walton, J. Sloan, Picoperovskites, The smallest conceivable isolated halide perovskite structures formed within carbon nanotubes, Adv. Mater. (2022), 2208575, https://doi.org/10.1002/adma.202208575.

[56] S. Stonemeyer, M. Dogan, J.D. Cain, A. Azizi, D.C. Popple, A. Culp, C. Song, P. Ercius, M.L. Cohen, A. Zettl, Targeting one- and two-dimensional Ta–Te structures via nanotube encapsulation, Nano Lett. 22 (2022) 2285–2292, https://doi.org/10.1021/acs.nanolett.1c04615.

[57] L. Shao, G. Tobias, Y. Huh, M.L.H. Green, Reversible filling of single walled carbon nanotubes opened by alkali hydroxides, Carbon N, Y (Dayt. Ohio) 44 (2006) 2855–2858, https://doi.org/10.1016/j.carbon.2006.06.010.

[58] M. Kierkowicz, E. Pach, J. Fraile, C. Domingo, B. Ballesteros, G. Tobias, The role of temperature on the degree of end-closing and filling of single-walled carbon nanotubes, Nanomaterials 11 (2021) 3365, https://doi.org/10.3390/nano11123365.

[59] M.V.A.U.-K. Kharlamova, ChristianTI - applications of filled single-walled carbon nanotubes: progress, challenges, and perspectives, No title, Nanomaterials 11 (2021) 2863, https://doi.org/10.3390/nano11112863.

[60] B. He, Y. Shi, Y. Liang, A. Yang, Z. Fan, L. Yuan, X. Zou, X. Chang, H. Zhang, X. Wang, W. Dai, Y. Wang, Q. Zhang, Single-walled carbon-nanohorns improve biocompatibility over nanotubes by triggering less protein-initiated pyroptosis and apoptosis in macrophages, Nat. Commun. 9 (2018) 2393, https://doi.org/10.1038/s41467-018-04700-z.

[61] M. Florensa, M. Llenas, E. Medina-Gutiérrez, S. Sandoval, G. Tobías-Rossell, Key parameters for the rational design, synthesis, and functionalization of biocompatible mesoporous silica nanoparticles, Pharmaceutics 14 (2022), https://doi.org/10.3390/pharmaceutics14122703.